Metals and Materials International (2021) 27:2743–2755
https://doi.org/10.1007/s12540-020-00842-2

Development of Ultrafine Grain Structure in an Al–Mg–Mn–Sc–Zr Alloy During High-Temperature Multidirectional Isothermal Forging

O. Sitdikov[1] · E. Avtokratova[1] · M. Markushev[1]

Received: 23 April 2020 / Accepted: 30 July 2020 / Published online: 17 October 2020

Abstract
Mechanisms of grain refinement under multidirectional isothermal forging (MIF) at 325 °C (~ 0.65 T_m) and the strain rate 10^{-4} s^{-1} of the Al–Mg-based alloy with complex additions of transition metals were investigated. The starting alloy had an equiaxed grain structure with grain size 25 µm and a uniform distribution of coherent Al_3(Sc,Zr) dispersoids of 20–50 nm. A distinguished structural feature in the early MIF stage was the formation of high strain- and misorientation gradients, followed by deformation banding. Due to the sequential changes of the loading axis, such bands were developed in various directions and fragmented the original grains. The number of bands and misorientation of their boundaries gradually rose with strain, resulting in formation of (ultra)fine grain structure with the grain size 2 µm. New grain formation was concluded to occur via continuous dynamic recrystallization and controlled by the nanosized precipitates, which preferably remained stable and coherent with the surrounding matrix.

Keywords Aluminum alloy · Severe plastic deformation · Grain refinement · Dispersoids

1 Introduction

One of the main scientific problems solved at the intersection of modern materials science, solid state physics and metal working is the development of new thermomechanical processing (TMP) techniques providing the improvement of both technological and service properties of commercial alloys, and particularly of aluminum-based alloys [1]. In this regard, much attention in the recent years was paid to the development of effective methods to control their structure–phase condition through processing of fine- and ultrafine-grained (UFG) structures (with grain sizes less than 10 and 1 µm, respectively). Pursuing these goals, new techniques were developed based on so-called severe plastic deformation (SPD), which consisted of repeated straining of the initial coarse-grain semi-finished products with the aim of introducing high strains and imparting to them the above mentioned structural states via activation of the processes of dynamic polygonization and/or recrystallization [1–4].

✉ O. Sitdikov
sitdikov@nm.ru

[1] Laboratory of Light Alloys, Institute for Metals Superplasticity Problems of Russian Academy of Science, Khalturin St. 39, Ufa, Russia 450001

Presently, there are a large number of studies published on grain refinement of metals and alloys during SPD, implemented by equal-channel angular pressing, multidirectional isothermal forging (MIF), high-pressure torsion, and other methods, as their combinations [5–17]. However, a detailed analysis of hardening and structuring during SPD, in particular, of high-temperature SPD of materials with high values of stacking fault energy, was carried out only in a few papers (for instance, in [7, 8, 11–15, 17]). There is a quite popular opinion, established since the early 2000s, that new grains upon SPD of such metals and alloys are formed mainly by the mechanism of continuous dynamic recrystallization [4, 10, 12, 14, 15, 17, 18]. However, the structural and phase factors controlling the grain refinement are still not so clear. Specifically, for aluminum alloys there are significant gaps in understanding the origin of processes, responsible for strain-induced development of new grains. Besides, the role of their alloying by transition metals (TM), that form intermetallic phases of various nature and dispersion, in the structuring of the matrix during SPD still remain undisclosed.

The aim of the present investigation was to study the microstructural development in the Al–Mg commercial alloy with complex additions of TM, subjected to MIF at elevated temperature (about 0.65 T_m) to elucidate the

formation feasibility of a UFG structure and analyze the mechanisms of grain refinement. The study may be particularly important for other complex alloys on different bases, whose treatment is often accompanied by premature failure and does not allow achieving high strains during SPD at low temperatures.

2 Material and Procedure

Modern commercial aluminum alloy 1570C (Al-5.0Mg-0.18Mn-0.2Sc-0.08Zr-0.002Be-0.01Fe-0.01Si, mass %) was chosen as a material for the study. The alloy belongs to new generation of high-strength non-age-hardenable wrought alloys. It can be easily hot worked, whereas its straining under ambient temperature can frequently lead to a failure due to high yield strength and relatively low ductility [19]. Commercial ingot was homogenized first at 360 °C for 6 h (first stage) and then at 520 °C for 1 h (second stage) in order to eliminate the liquation of Mg and dissolve the non-equilibrium Al_3Mg_2/Al_8Mg_5 constituent phase. Rectangular samples of 18 mm × 17 mm × 10 mm cut from the ingot were subjected to multidirectional compression with changing the loading direction by 90° from pass to pass under isothermal conditions at 325 °C and the strain rate of 10^{-4} s^{-1}. The total accumulative strain, $e = \Delta e_1 + \Delta e_2 + \Delta e_3 + \ldots + \Delta e_n$, where $\Delta e_n = ln(H_n/h_n) = 0.7$ was the true strain and H_n was the initial- and h_n was the final specimen height in each compression pass [20], was applied up to 8.4.

The microstructural analysis was performed in the central part of the samples in a section parallel to the last loading direction using Nikon L-150 optical microscope. Prepolished samples were etched in a Keller's reagent. Orientation imaging scanning electron microscopy (OIM-SEM) maps and distributions of misorientations of (sub)boundaries were obtained from electron backscattered diffraction (EBSD) analysis using TESCAN MIRA 3 LMH scanning electron microscope equipped with a field-emission gun and HKL Channel 5 software [21]. It was run in a high vacuum mode at 20 kV with a current of beam of approximately 2.2 nA. The scan area in EBSD analysis was varied from 100 × 100 to 200 × 200 μm^2 depending on the homogeneity of the structure analyzed. The scanning step size was 0.1–0.25 µm depending on the length scale and the area of interest. A standard procedure of "noise reduction" was applied to clean up non-indexed points [21], the fraction of which did not exceed 25%. Different grey-scale levels in the EBSD maps indicated various crystal orientations. The low-angle boundaries (LABs) that corresponded to the angles of misorientation between adjacent scan pixels, $2° \le \Theta < 5°$, and medium-angle ones with $5° \le \Theta < 15°$ were marked by thin light-grey and dark-grey lines, while the high-angle boundaries (HABs) with $\Theta \ge 15°$ were indicated in the maps using thick black lines, respectively. Among the boundaries indicated those with misorientation angles less than 2° were not taken into consideration. Transmission electron microscopy (TEM) was carried out by JEOL-2000EX microscope. Specimens for SEM and TEM were electropolished using Tenupol-5 twin-jet polishing unit at 20 V and temperature of -28 °C in a solution of 30% HNO_3 and 70% CH_3OH.

The sizes of new (sub)grains were derived from the SEM-EBSD and TEM analyses by conversion of the measurements of the areas of crystallites into "circle equivalent diameters" [21, 22] with averaging of the "equivalent diameters" of each distinct crystallite. The size of precipitates $Al_3(Sc,Zr)$ and their distribution were determined using dark-field TEM image analysis [23, 24]. The secondary phase number density was measured as the ratio of the number of precipitates per unit of the TEM image area and the thickness of a foil. The latter was evaluated by extinction contours appearing on the grain boundaries [23]. Besides the above mentioned scanning and transmission electron microscopes were equipped with energy dispersive X-ray spectrometers, which were used for composition analyses of intermetallic phases. The room-temperature Vickers microhardness (HV) was determined by semi-automatic "Metrotest" device at a load of 0.5 N.

3 Results and Discussion

3.1 Initial Structure

The microstructure of the starting material is shown in Fig. 1. It can be seen that it was homogeneous, consisting of equiaxed grains with average size of about 25 µm (Fig. 1a–c) and prevailed high-angle intergranular boundary spectrum with the average misorientation angle about 39° (Fig. 1d). In the TEM structure, nanosized uniformly-distributed $Al_3(Sc,Zr)$ precipitates with a diameter of 20–50 nm and a number density of 5×10^3 μm^{-3} were observed in the dark-field images taken in appropriate $Al_3(Sc,Zr)$ reflection (Fig. 2a). Note that in the selected electron diffraction pattern supplied, strong reflection spots due to the Al-matrix were clearly visible, while fine spots of $Al_3(Sc,Zr)$ precipitates were appeared at around 1/2 -typed positions of the matrix reflexes. This suggested that these precipitates were fully coherent within the matrix [23, 24]. Also, their coherency with the matrix was testified by their delta-zero contrast [23] in the bright-field TEM images (Fig. 2b). Besides, some small quantities of the excess and secondary phases, presumably of $Al_6(Fe,Mn)$ up to 3 µm and Al_6Mn up to 300 nm, that were conditioned by relatively low contents of Mn and Fe in the present alloy [15, 25], were detected with local variations in density in the grain-boundary regions and in the grain bodies, respectively (see Figs. 1b, 2c, d).

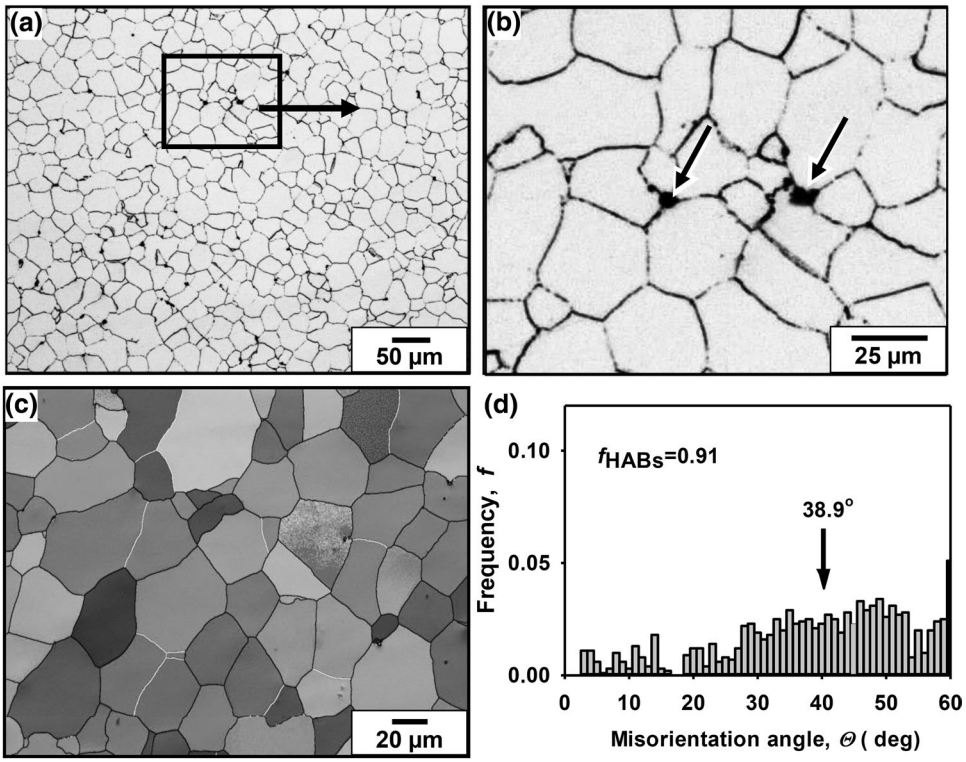

Fig. 1 Initial microstructure of the aluminum alloy 1570C after homogenization: **a**, **b** optical microscopy: **b** shows enlarged portion outlined in **a**; **c** EBSD map; **d** misorientation spectrum of intercrystallite boundaries; the excess phases at the original grain boundaries are arrowed in **b**

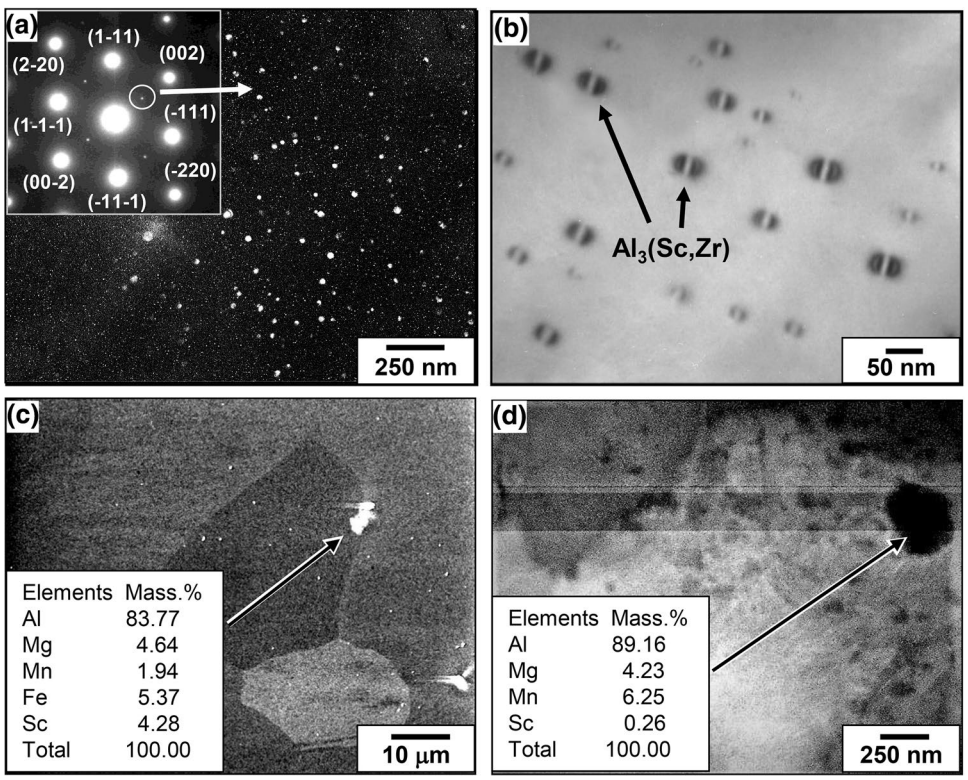

Fig. 2 Typical examples of the second phases in the aluminum alloy 1570C after homogenization: **a** dark-field TEM image in Al_3(Sc,Zr) reflection, indicated in selected area diffraction pattern supplied; [110] zone axis; **b** bright-field TEM image of precipitates Al_3(Sc,Zr); **c** SEM and **d** TEM images and corresponding chemical compositions of the excess phases Al_6(Fe,Mn) and precipitates Al_6Mn, respectively

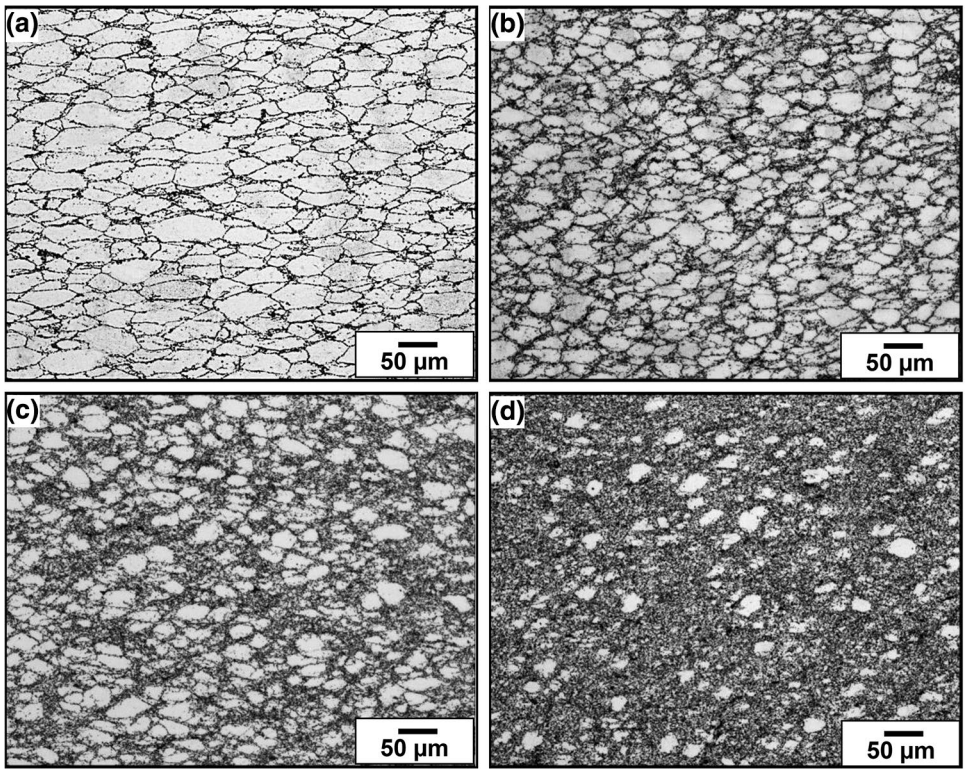

Fig. 3 Typical optical microscopy structures of the aluminum alloy 1570C subjected to MIF: **a** $e = 0.7$; **b** $e = 2.1$; **c** $e = 4.2$; **d** $e = 8.4$. The last compression axis is vertical

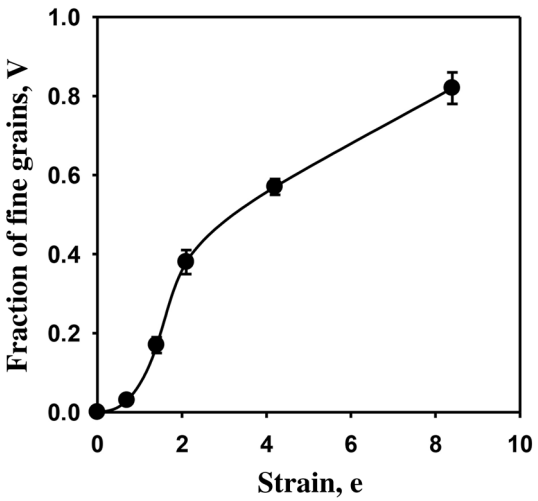

Fig. 4 Volume fraction of fine grains developed in the aluminum alloy 1570C after MIF to different strains

3.2 MIF Processed Microstructure

The microstructural evolution under MIF is represented in Fig. 3. It is seen that in the early stages of deformation ($e = 0.7$), the initial grains were somewhat elongated and flattened in the direction perpendicular to the compression axis (Fig. 3a) and then partially restored their equiaxial shape after completion of the full MIF cycle (i.e. at $e = 2.1$) (Fig. 3b). Simultaneously, the new fine grains (dark regions in Fig. 3) were formed in the vicinity of old grain boundaries. At $e = 1.4$ and $e = 2.1$, the fractions of such grains were as high as 0.17 and 0.38, respectively (Fig. 4). Therewith, so-called "necklace-like structures" consisted of coarse initial grains surrounded by regions of new fine grains were evolved in the alloy. Note that such structural phenomenon looks similar to that observed upon the discontinuous ("necklace-type") dynamic recrystallization, which frequently takes place during a high-temperature straining of low- and medium stacking fault energy materials [4]. However, their mechanisms of structuring are non-identical, as it will be discussed below.

With further strain increase (Fig. 3c, d), the fine grain regions progressively occupied the original grain interiors. Their volume fraction reached 0.57 at $e = 4.2$ and 0.82 at $e = 8.4$ (Fig. 4) and resulted firstly in a bimodal, and then in almost uniform (ultra)fine-grain structure. Thus, a profound grain refinement took place during high-temperature MIF of the present alloy.

More detailed study by means of EBSD analysis (Fig. 5) showed that at all strains investigated, the alloy microstructure contained the networks of LABs, which constituted the dynamically equilibrium subgrain structure [26–28]. Besides, a distinctive feature of the microstructure developed under initial MIF stages (Fig. 5a, b) was the formation of significant deformation/orientation gradients, as well as medium-angle boundaries, which bounded the deformation

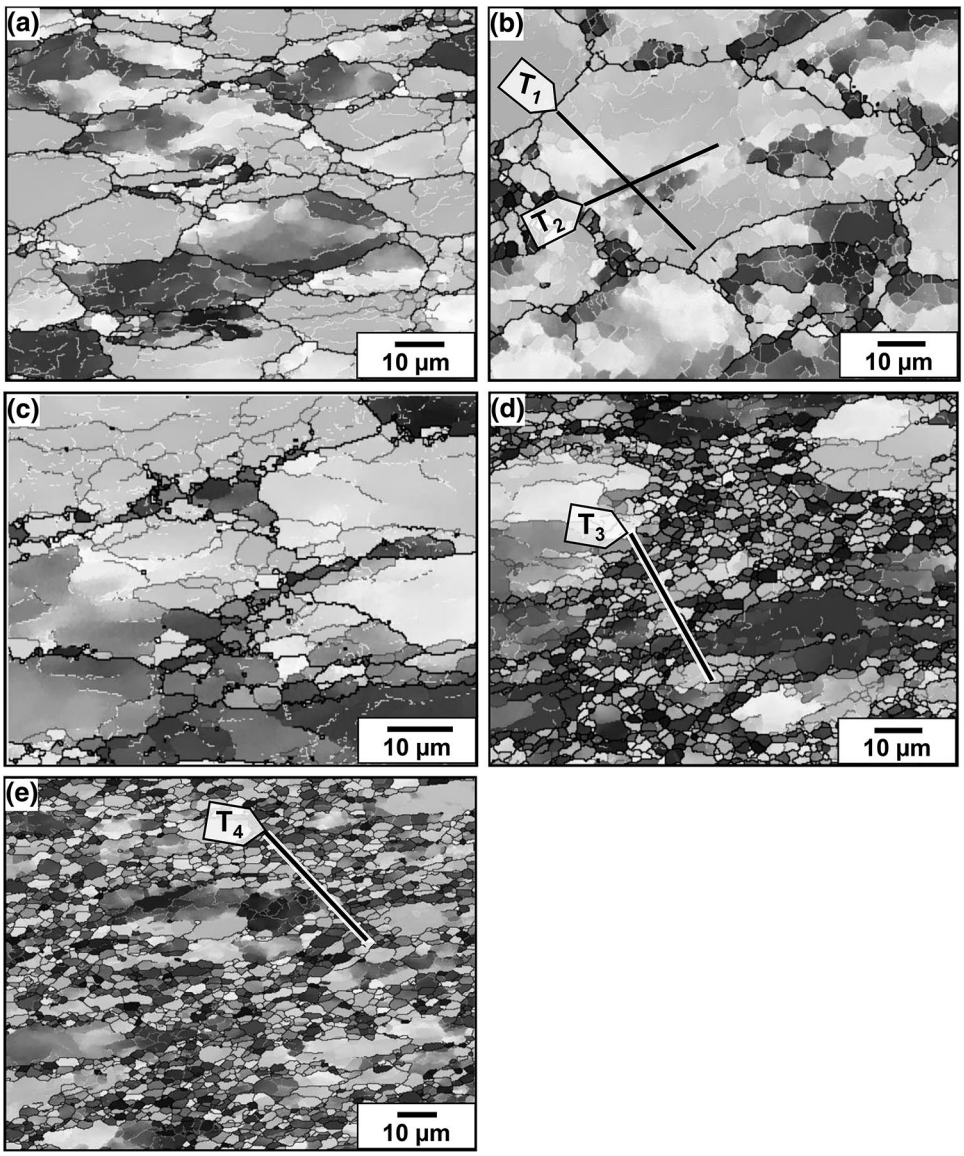

Fig. 5 Typical EBSD maps of the aluminum alloy 1570C subjected to MIF: **a** $e = 0.7$; **b** $e = 1.4$; **c** $e = 2.1$; **d** $e = 4.2$; **e** $e = 8.4$. The last compression axis is vertical

bands. The latter resulted in fragmentation of original grains; similar to that observed at low SPD temperatures [4, 13, 29–31]. This implies that along with thermally-activated processes, related to dynamic recovery [4], some athermal mechanically-induced processes, caused by strain localization and local lattice rotations [29], could play an important role in the structure changes during high-temperature MIF of the present alloy.

Figure 6a and b shows the changes in crystallographic orientation between neighboring points ($\Delta\Theta$ is the point-to-point misorientation) and those with respect to the starting points ($\Sigma\Delta\Theta$ is the cumulative misorientation) along the lines T_1 and T_2, respectively, selected in Fig. 5b. It can be seen that in the early stages of deformation (with $e \leq 1.4$), $\Delta\Theta$ inside the grain were mainly less than 5°, which corresponded to the boundaries of subgrains with low-angle misorientations [26, 28]. At the same time, some boundaries, corresponded to those of the deformation bands in Fig. 5b, had a misorientation angle of 8–10°, while the cumulative misorientation has changed stepwise and alternated at them (Fig. 6a, b). Thus the data obtainable from the linescans showed that the material orientation in interiors of the deformation bands was rotated considerably away from the adjacent matrix, whilst the matrix which they fragmented remained at a common orientation. This suggested that the inhomogeneous deformation developing in the alloy led to local lattice rotations, akin to kinking [29] and, as a result, the formation of dislocation subboundaries with medium-to-high misorientations. It should be noted that such the structural behavior was quite similar to that of microshear bands reported for cold rolling or equal-channel angular pressing of an aluminum alloy [13, 29], which were also observed in

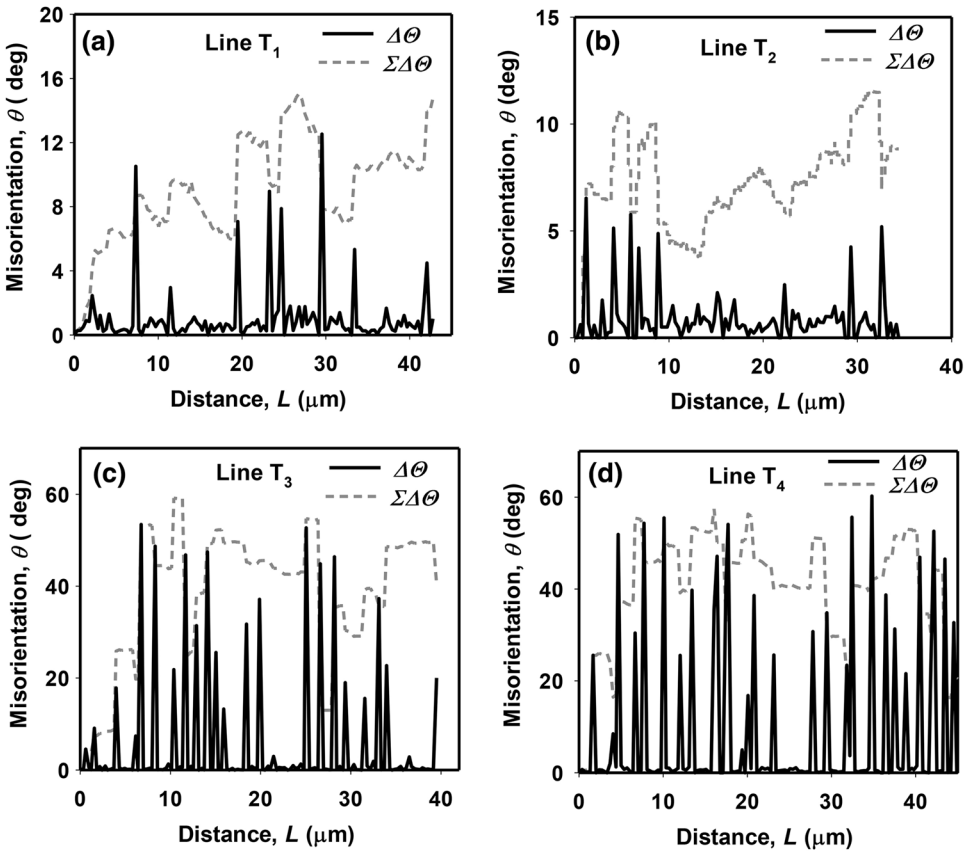

Fig. 6 Point-to-point ($\Delta\Theta$) and cumulative ($\Sigma\Delta\Theta$) misorientations along the lines: a T1; b T2; c T3; and d T4 highlighted in Fig. 5 b, d and e

some complex-alloyed materials even at deformation at elevated temperatures [12, 14, 17, 18]. Like under cold rolling [29], this allowed demonstrating clear differences between the misorientations introduced into the deformed structure by the boundaries of deformation/microshear bands and those of "ordinary" cellular/subgrain structures, formed by dynamic recovery [27–29]. By the way, significantly lower misorientations were developed in the long direction inside the bands, as shown by the data obtained along the line T_2 (Fig. 6b). It can also be seen that the point-to-point misorientations along this line were higher near the old high-angle boundary than those in the grain body. This indicated that more significant lattice rotations occurred along these initial boundaries. As a result, it was easier for individual fine crystallites, surrounded by high- and medium-angle boundaries, to form first near the boundaries of the original grains (Fig. 3), where the preferred formation of deformation bands with higher-angle boundary misorientations was detected.

During subsequent deformation ($e = 2.1$), a large number of moderate-angle boundaries, which misorientation angles were mainly varied from 5 to 15º, were formed in the alloy microstructure (Fig. 5c). Due to a periodic change in the loading axis in the MIF, these boundaries developed in different directions and, accordingly, intersected and fragmented the initial grains [30, 31].

With a further increasing the strain, the density of the strain-induced boundaries became larger; that led to the formation of areas of new fine grains. Figure 6c and d displays the variations of $\Delta\Theta$ and $\Sigma\Delta\Theta$ along the lines T_3 and T_4 in typical grain structures in Fig. 5d, e developed at the strains of $e = 4.2$ and $e = 8.4$, respectively. One can see that in comparison to the data in Fig. 6a and b, the $\Delta\Theta$ for the most deformation-induced boundaries grew up to the values corresponding to HABs, while their densities increased gradually by MIF processing to develop the uniform fine–grain structures. After the strain of 8.4 (Fig. 5d), the fraction of HABs was about 0.75 with an average misorientation angle of intercrystallite boundaries of about 30º. Thus, the density and misorientation angle of dislocation subboundaries, such as boundaries of deformation bands, increased with deformation, providing fragmentation and refinement of the grain structure in the alloy.

However, some coarse fragments of initial grains still survived under SPD even at e, exceeding 8. Such a behavior can be caused by the fact that the deformation energy applied to the billet at high strains can be almost completely relaxed and dissipated by the formed (ultra)fine–grain matrix (e.g. due to easy occurrence of dynamic recovery and grain boundary sliding in fine grained regions under high-temperature deformation [13–15, 17, 18]). By the way, the interiors of coarse remnant grains after high MIF strains

of an aluminum alloy were separately analyzed by EBSD in the previous authors' work [32]. The results showed that the average misorientation angle of the boundaries developed in these grains did not exceed 5°. This suggests that conventional subgrains with LABs can remain stable and do not transform into ultrafine grains. Any strain gradients (and deformation bands) were not developed in these remnant grains because of a weak plastic constraint from the surrounding fine grains, as mentioned above. The subgrains in the remnant grains may correspond to "dynamically equilibrium subgrain structure" evolved during steady state flow in many aluminum alloys under conventional warm or hot deformation conditions [4, 26–28].

The alloy microtexture derived from EBSD analysis is represented in Fig. 7. In this figure the positions of the compression axis (CA), as well as the normal direction (ND) and transverse direction (TD) of the sample were sequentially changed from pass to pass during MIF. It was found that the deformation of the fcc-material in each compression pass tended to ensure the lattice rotation towards a stable orientation (<110> // CA) [33, 34] (see, e.g., Fig. 7a). But this rotation periodically redirected during MIF upon changing the CA direction (Fig. 7b, c). This suggested that any stable grain orientation, that was formed within the previous pass, was destroyed during the next pass; that, probably, stimulated additional development of the deformation bands and

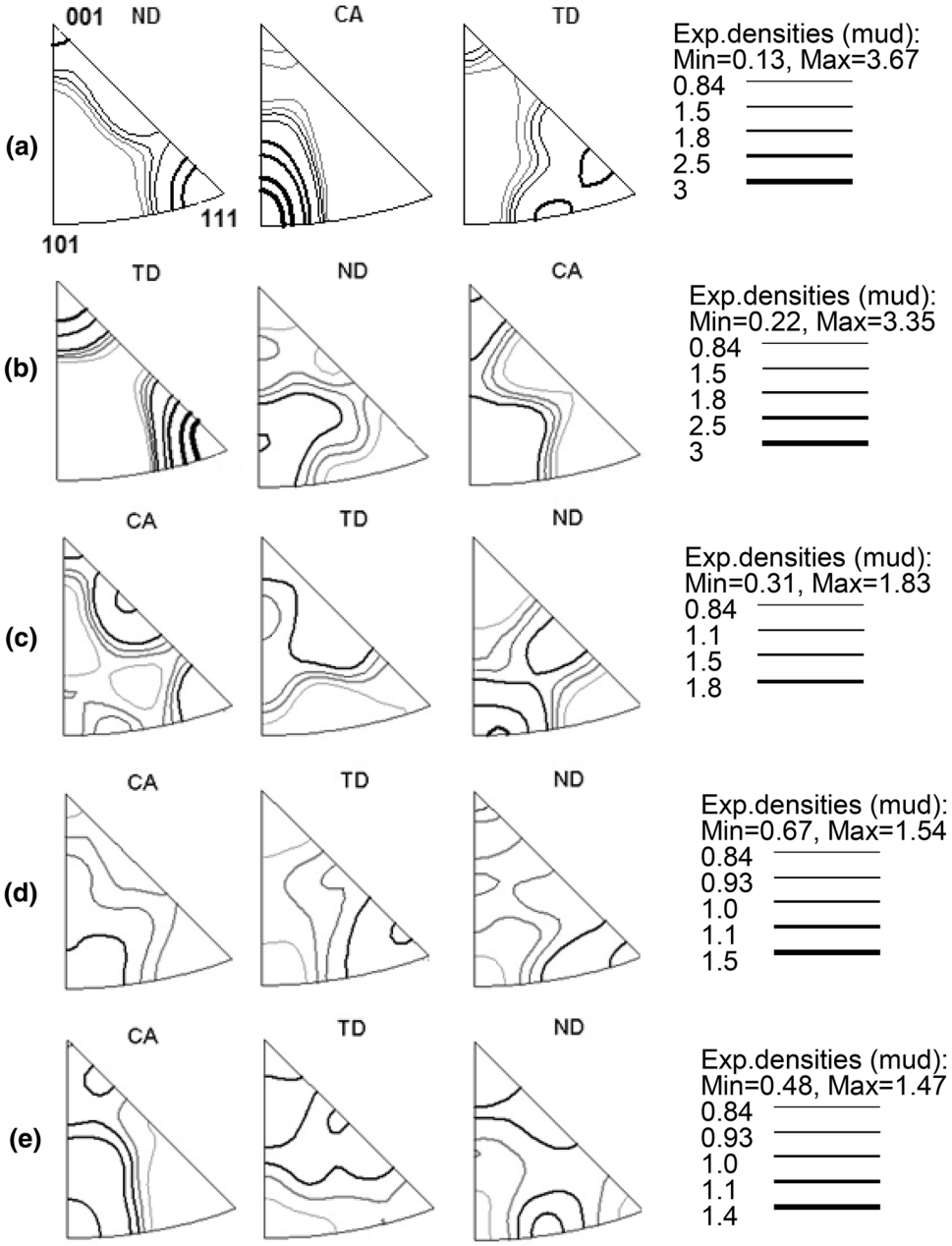

Fig. 7 Changes in the texture of the aluminum alloy 1570C subjected to MIF: **a** $e = 0.7$; **b** $e = 1.4$; **c** $e = 2.1$; **d** e=4.2; **e** $e = 8.4$

grain fragmentation [4]. Also, appearance of some maximums of orientations near the poles <001> and <111> was revealed at low-to-moderate strains (Fig. 7c). Such changes could be associated with the local reorientation of the crystal lattice and formation of new grains during MIF. With an increase in the number of passes, a gradual decrease in the intensity maximum from 3.7 at $e = 0.7$ to 1.4 at $e = 8.4$ was observed (Fig. 7e); that indicated a weakening the texture during hot deformation caused by development of new grains and randomization of their orientations [17, 18] with strain (Fig. 5e).

3.3 TEM Structures

TEM microstructures of the alloy are shown in Figs. 8, 9, 10 and 11. In the early stage of deformation ($e \leq 2.1$), mutually intersected deformation bands containing rather coarse rectangular crystallites were developed in the material structure (Fig. 8a, b). It should be noted that despite a rather high deformation temperature, high densities of lattice dislocations were frequently observed in local areas of such a structure. Also the azimuthal spreading of the diffraction points in the supplied selected angular diffraction patterns suggested that rather large local lattice rotations and internal stresses can be developed in the strain-induced structure at low strains [23]. With further strain increasing, the number of mutually intersecting deformation bands gradually raised (Fig. 8c), and the restricted migration of intergranular boundaries also took place. As a result, the crystallites tended to approach the equiaxed shape with angles at the triple junctions close to 120° (Fig. 8d). This indicates that the alloy structure became more equilibrium at high strains. Therewith, the diffraction patterns showed almost uniform discrete rings (Fig. 8c, d), suggesting that the microstructure evolved was composed by crystals surrounded by medium-angle boundaries and HABs.

Thus, TEM data independently confirmed the fact that the development of strain / misorientation inhomogeneities that lead to the development of deformation bands played an important role in grain refinement of the alloy structure during high-temperature MIF. Note in this regard that the origin of the deformation banding is not entirely clear now [4]. It is known that deformation bands can develop in the grain interiors due to various types of plastic constrains that can be caused by material-deformation conditions, e.g. such as strain compatibility requirements by neighboring grains, etc. [4, 14, 29]. Under cold deformation conditions, deformation bands are frequently formed, because it is easier to deform the grain, if it is subdivided into the areas, where the number of slip systems required for limited deformation is less than 5. Deformation bands subsequent to grain fragmentation can also be developed as a result of the (micro)shear banding originated from some plastic/geometric instability due to the inability of the material to sustain further work hardening [35], or it is equally likely that they may originate from

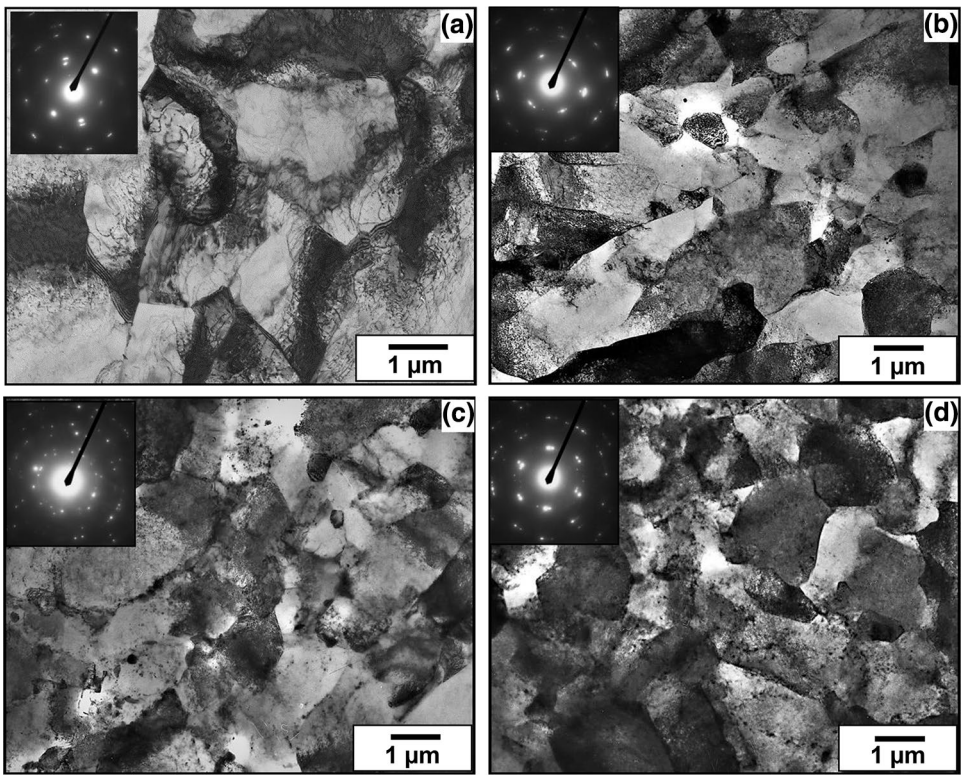

Fig. 8 Typical TEM structures of the 1570C aluminum alloy subjected to MIF to **a** $e = 0.7$; **b** $e = 1.4$; **c** $e = 4.2$; **d** $e = 8.4$. Selected area diffraction patters supplied were taken from the areas with diameter 5 μm

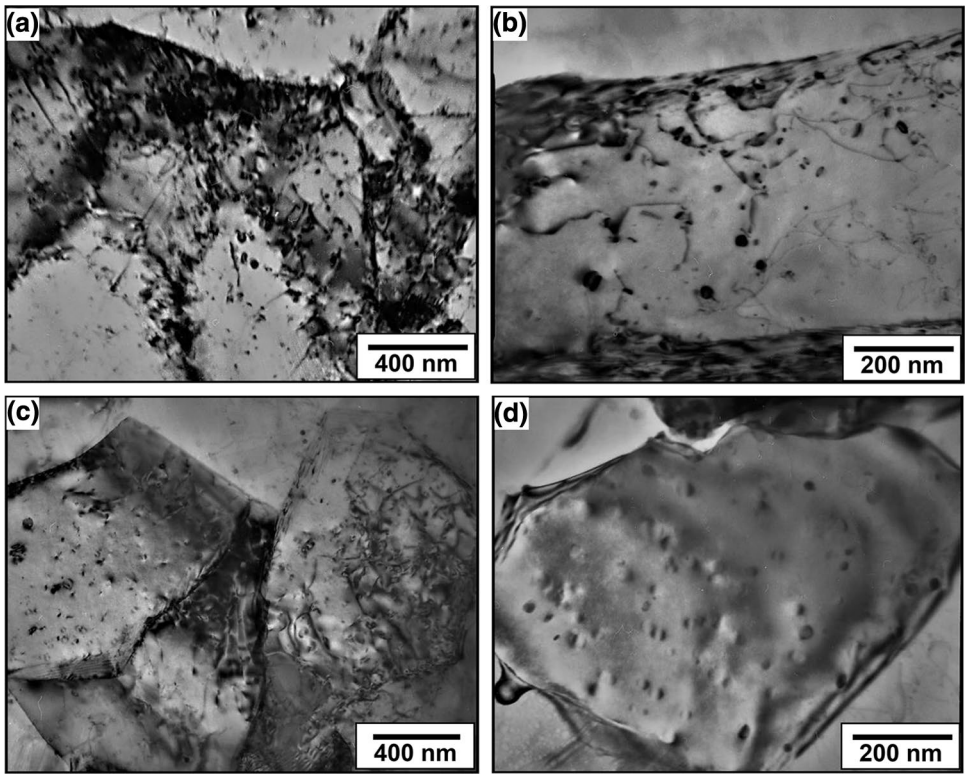

Fig. 9 TEM structures of the aluminum alloy 1570C subjected to MIF to **a** $e = 1.4$; **b**, **c** $e = 2.1$; **d** $e = 4.2$

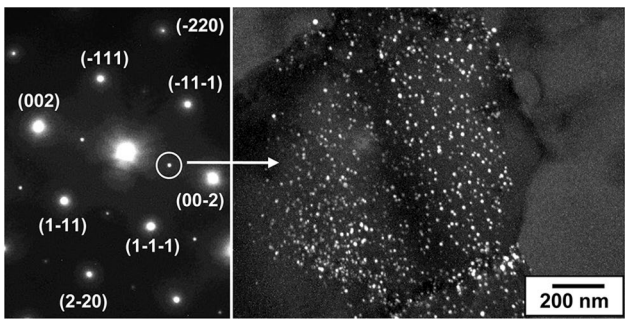

Fig. 10 Dark-field TEM image in $Al_3(Sc,Zr)$ reflection indicated in selected area diffraction pattern obtained for the aluminum alloy 1570C subjected to MIF to $e = 8.4$; [110] zone axis

certain combinations of slip systems as assumed in [36]. At last, some external constraints can also appear at the macroscopic level as an unavoidable consequence of interaction between the sample and the tool, for example, due to friction during metalworking. It is obvious [4, 14] that when a sample is deformed in accordance with any external constraints, different macroscopic strains must develop in different parts; this can lead to severe inhomogeneous deformation throughout the whole volume, as well as in the interior of the grain and thus, to the development of microstructural inhomogeneity followed by the formation of deformation bands.

It should be, however, noted that the above result, obtained for a complex-alloyed aluminum alloy, may not be typical for other low- and moderate-alloyed alloys [14, 37, 38], since it is known that the high-temperature deformation of the latter cannot provide favored conditions for localization of plastic flow and intense formation of deformation bands [14, 37]. Namely, the dislocation glide becomes more homogeneous at high temperatures, and even if high deformation- and/or misorientation gradients could occur in the initial grains, they would quickly disappear due to the high rate of relaxation processes, such as dynamic recovery or grain-boundary sliding [4, 27, 39]. Thus, the formation of new grains during SPD of these alloys should be suppressed with an increase in the deformation temperature above $0.5\,T_m$.

However, the present alloy contained high densities of nanoscale coherent precipitates of TM aluminides (Fig. 2), stabilizing its structure. Such nanosized particles, mostly exhibiting the delta-zero contrast in the bright field and virtually unchanged dispersity in the dark field after various stages of MIF, can be seen in Figs. 9, 10 and 11. Also characteristic distribution features of the fine reflection spots of $Al_3(Sc,Zr)$ precipitates in the 1/2-type positions of the strong spots of the Al matrix can be still clearly seen even after $e = 8.4$ in an enlarged diffraction pattern shown in Fig. 10a. This suggests that the precipitates remained mainly stable during high-temperature SPD and did not lose their coherency with the surrounding matrix. In addition, it is evident in Fig. 9 that the lattice dislocations as well as the boundaries of new evolved (sub)grains frequently interacted with

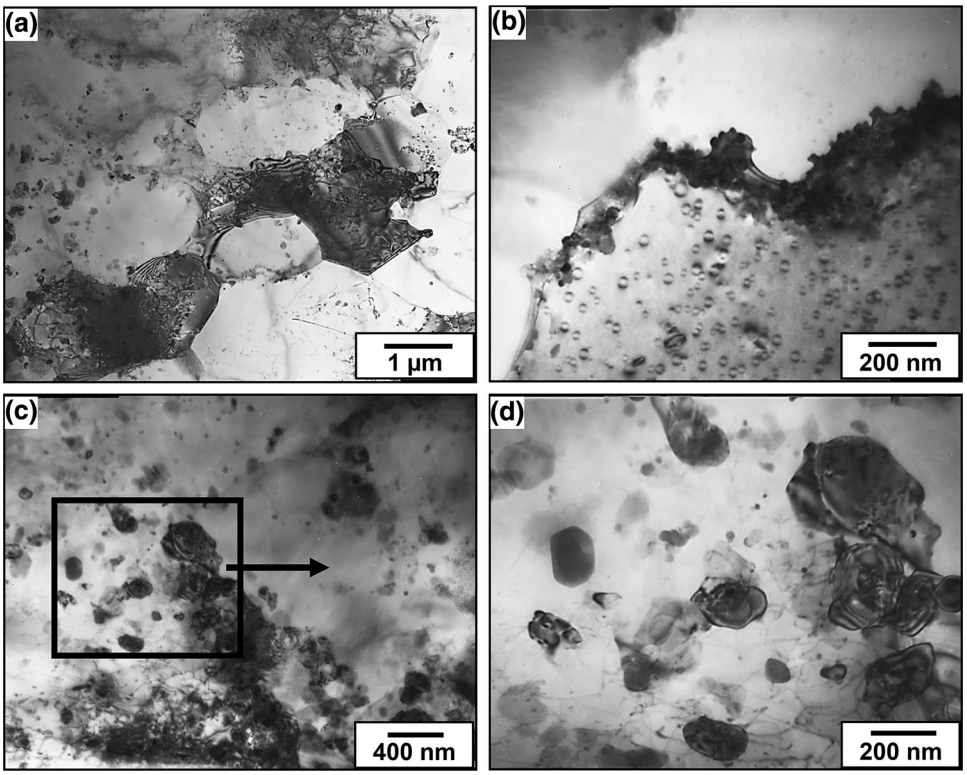

Fig. 11 **a**–**d** TEM structures of the aluminum alloy 1570C subjected to MIF to $e = 8.4$: **d** shows enlarged portion outlined in **c**

these precipitates. Relying upon these observations, it can be assumed that the compact nanosized phases hindered the rearrangement of dislocations at high temperatures, thereby preventing their annihilation under high-temperature dynamic recovery [13, 15, 40, 41]. Also the particles, which pinned the grain boundaries, impeded their migration on long-distances. Apparently, these factors could be largely responsible for the evolution of the microstructure and grain refinement at hot deformation. At the same time, much coarser precipitates were found in some grain boundary regions after high straining (Fig. 11a, b). The latter also were of compact shape with much larger diameter, than those in grain interiors. This suggested that some intense coarsening of the aluminides took place in the grain boundary regions. The most common reasons for such a coarsening can be the loss of coherency of the precipitates owing to their interaction with the HABs, as well as the higher diffusion rate of dissolved atoms of Zr and Sc along HABs, as it can be compared to the grain bodies [40, 41].

Also, it was interesting to find by means of TEM that along with the abovementioned grain fragmentation mechanism, there was the nucleation of new grains near some coarsest precipitates in the grain boundary vicinities (Fig. 11c, d). These nuclei were probably formed by dynamic recrystallization, occurred in discontinues manner due to particle stimulated nucleation [4]. They tended to rapidly grow, but were stopped at a fairly small size of about 100–150 nm by the surrounded finer phases (Fig. 11d). It is also important to note in this way that in contrast to the present alloy/deformation conditions, no such discontinuous grain nucleation was detected in the similar 1570C alloys during hot MIF and/or equal channel angular pressing at higher strain rates [40, 41]. Such difference can appear from the effect of the magnesium atoms atmospheres present in the aluminum solid solution and arise also from the difference in strain rates, promoting different micromechanisms of plastic flow [39, 42]. Namely, the solute atmospheres at high strain rates were left behind the moving dislocations due to higher dislocation velocities, providing the dislocation densities, which were too low to start nucleation of new grains. But at the low strain rates of about 10^{-4} s^{-1}, the dislocation motion was slowed by a higher solute dragging [39]. This can lead to higher stored dislocation densities to initiate dynamic recrystallization [26, 42]. Note, however, that the contribution of this mechanism of dynamic recrystallization to the total grain refinement was negligibly small, since the amounts of Mn, Fe and other impurities was strongly restricted in the present alloy [25]; that resulted in the low number of the coarse second phase particles, suitable for the grain nucleation. Thus, the particle stimulated nucleation was detected only at the highest investigated strain of $e = 8.4$, while the volume fraction of nuclei was too small (only 2%–3%) to play any significant role in the alloy structural behavior.

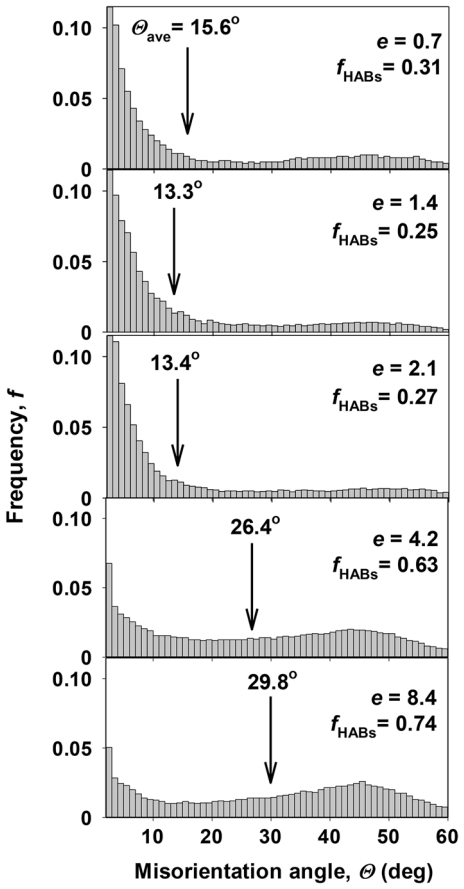

Fig. 12 Misorientation distributions at intercrystallite boundaries in the aluminum alloy 1570C developed during MIF to different strains

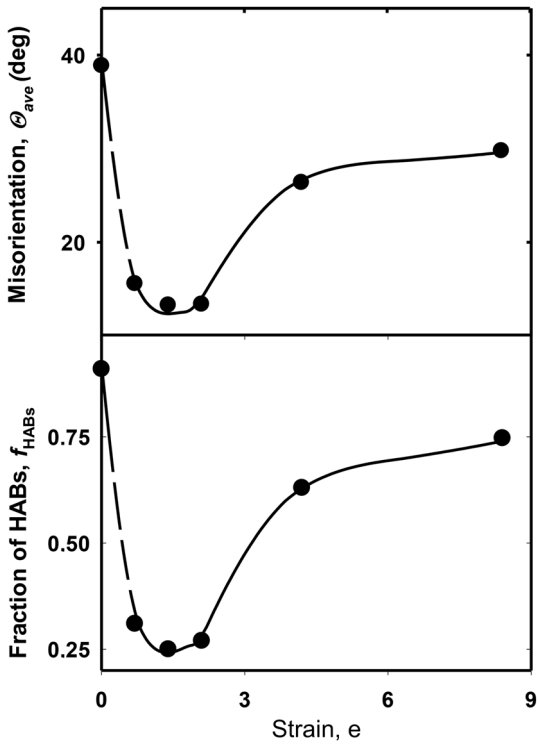

Fig. 13 Strain dependences of the average misorientations of intercrystallite boundaries and the fraction of HABs developed in the aluminum alloy 1570C during MIF

3.4 Parameters of the Evolved Microstructure

Figure 12 shows the alloy (sub)grain boundary spectrums along with the average misorientation angles (Θ_{ave}) and HABs fractions (f_{HABs}) after MIF to different strains. It can be seen that in the early stages of deformation ($e = 0.7$–2.1), the alloy structure was characterized by roughly similar distributions of boundary misorientations, being frequently observed upon low-temperature SPD of metals with a cubic lattice [10, 30]. Namely, along with the LABs, a significant number of the strain-induced boundaries exhibited medium-angle misorientations, that corresponded to the boundaries of the deformation bands, as described above. With further straining to e of beyond 2.1, the fractions of HABs increased (Fig. 12), which is due to the transformation of medium-angle boundaries into HABs and the formation of new fine grains.

The kinetics of grain refinement is illustrated in Fig. 13. As can be seen, at low strains the angular parameters of the structure decreased owing to the formation of a substructure in the initial cast material (Fig. 5a, b). At medium strains, they rapidly increased, due to both an increase in the number of deformation bands and transformation of their boundaries into HABs (Fig. 5c, d) [43]. And at large strains, the development of deformation bands was suppressed since the coarse-grained regions gradually disappeared by a progressive grain refinement (Figs. 4, 5d, e). Hence, grain refinement at these strains can be controlled by the transformation

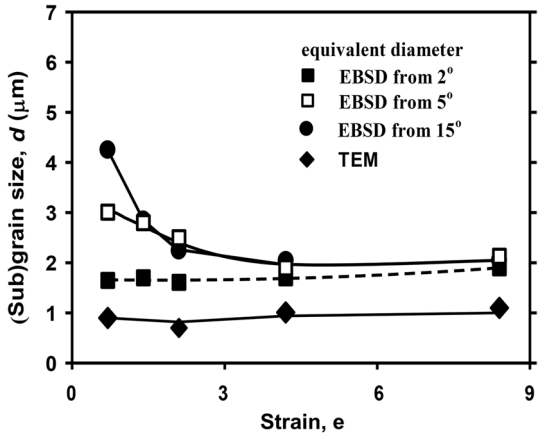

Fig. 14 Dependences of the mean size of deformation-induced (sub) grains developed in the aluminum alloy 1570C during MIF versus strain

of the earlier introduced deformation bands into HABs only. As a result, the growing rates of the angular parameters of the microstructure slowed down and they are saturated at high strains at approximately constant values of f_{HABs} and Θ_{ave} [43].

Figure 14 shows the dependences of the average size of deformation-induced (sub)grains on the MIF strains. According to data derived from the EBSD analysis, the sizes of the crystallites, surrounded by boundaries of deformation bands and HABs with moderate- and high-angle misorientations from 5° and 15°, respectively, initially decreased and then stabilized at approximately 2 µm at a certain strain. At the same time, the size of subgrains with low-angle misorientations (from 2°) remained almost constant and approached to 1.7–1.8 µm. Meanwhile, it is worth noting that the crystallite sizes derived from TEM were as high as 1-1.2 µm, i.e., smaller than those from the EBSD analysis. This can be explained by the fact that the EBSD analysis did not take into account the subgrain boundaries with a misorientation of less than 2°. On the other hand, the EBSD analysis can certainly provide more accurate crystallite size measurements, owing to much better statistics than TEM [29].

The character of the dependences in Figs. 12, 13 and 14, when the grain size corresponded approximately to that of (sub)grain size and the average misorientation of boundaries continuously increased with strain, suggested the new grain structure development during MIF of the present alloy in accordance to the mechanisms of continuous dynamic recrystallization [4].

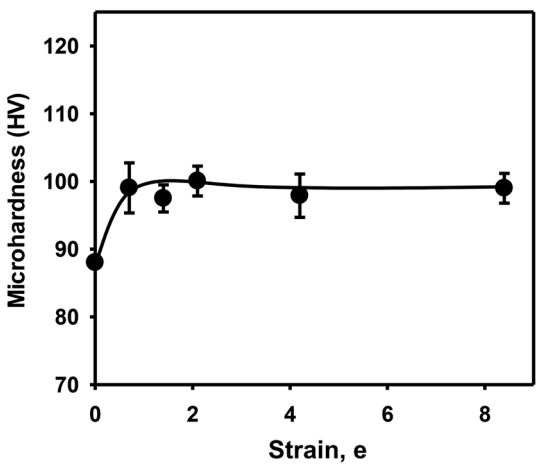

Fig. 15 Dependence of the room–temperature Vickers microhardness of the aluminum alloy 1570C on the MIF strain

3.5 Microhardness Changes

Figure 15 represents the dependence of the microhardness of the alloy 1570C on the MIF strain. It is seen that the alloy did not generally loose its high strength after thermomechanical processing at the elevated temperature. This can be probably attributed to the large number of precipitates that remained coherent, nano-dispersed and evenly distributed in the microstructure (Figs. 9, 10, 11). Moreover, the alloy hardness increased from approximately 90 to 100 HV at $e = 0$–0.7, which can be explained by its deformation/substructural hardening due to increase in the dislocation density and formation of well-developed (sub)grain structure (Figs. 5, 8a) [44]. With a further increase in strain, in spite of quite intense grain refinement (Fig. 3), the MIF did not result in the alloy sense strengthening and the microhardness remained almost unchanged and averaged at about 100 HV. It should be noted that such a saturated stress-strain behavior of the microstructure processed by high-temperature MIF, can be similar to flow curves of some cubic metals with high stacking fault energy strained at medium-to-high temperatures [26, 27] and mainly controlled by the dynamic recovery, resulting in the development of the dynamically-equilibrium subgrain structure [4, 26–28]. This suggests that the main restoration mechanism operating during continuous dynamic recrystallization is principally dynamic recovery, when the formation of the equilibrium subgrain structure, rather than (ultra)fine–grain development can be mainly responsible for the alloy hardening behavior after hot deformation.

4 Conclusions

1. Fairly uniform (ultra)fine–grain structure with the grain size of about 2 µm and the subgrain size of about 1–1.2 µm can be processed in a complex and hard-to-deform aluminum alloy 1570C by the MIF at a temperature of 325 °C (~ 0.65 T_m) and the strain rate of 10^{-4} s^{-1}.
2. The main mechanism of grain refinement was related to the formation of deformation bands which developed in different directions and fragmented the initial grains. A gradual increase in the number of bands and misorientation of their boundaries with increasing the strain led to the transformation of the latter to HABs and the formation of a fine–grained structure. Such mechanism of the formation of new grains in the present alloy was similar to "continuous" dynamic recrystallization.
3. The present alloy contained a respectable amount of nanoscale coherent precipitates $Al_3(Sc,Zr)$, that remained mainly stable during high-temperature MIF and stabilized its microstructure. In particular these nanodispersed phases hindered the rearrangement of dislo-

cations and dislocation boundaries at high temperatures, thereby preventing their annihilation by dynamic recovery. They can also pin the grain boundaries and impede their migration on long-distances. These factors may be largely responsible for the evolution of the deformation bands and grain refinement during high-temperature deformation.

4. Since most of the dispersoids remained coherent, nanoscale and uniformly distributed in the structure, the alloy retained high strength after thermomechanical processing. Moreover, the microhardness of the alloy slightly increased after the early stages of MIF, followed by its saturation at higher strains. This was caused by substructural hardening during severe plastic deformation.

Acknowledgements The work was supported by the Russian Science Foundation under Grant No. 16-19-10152-P and the Ministry of Science and Higher Education of Russia in accordance to the state assignment of IMSP RAS under Grant AAAA-A19-119021390107-8 (composition analyses of intermetallic phases). The authors are grateful to Dr. M. Shagiev for the useful discussions and Mr. B. Atanov for help in experimental work.

References

1. R.Z. Valiev, R.K. Islamgaliev, I.V. Alexandrov, Prog. Mater Sci. **45**, 103 (2000)
2. R.Z. Valiev, T.G. Langdon, Prog. Mater Sci. **51**, 881 (2006)
3. M.V. Markushev, Lett. Mater. **1**, 36 (2011)
4. F.J. Humphreys, M. Hatherly, *Recrystallization and Related Annealing Phenomena*, 2nd edn. (Elsevier Ltd., New York, 2004), p. 605
5. K. Nakashima, Z. Horita, M. Nemoto, T.G. Langdon, Acta Mater. **46**, 1589 (1998)
6. P.B. Berbon, M. Furukawa, Z. Horita, M. Nemoto, T.G. Langdon, Metall. Mater. Trans. A 30, 1989 (1999)
7. A. Yamashita, D. Yamaguchi, Z. Horita, T.G. Langdon, Mater. Sci. Eng. A **287**, 100 (2000)
8. C. Pithan, T. Hashimoto, M. Kawazoe, J. Nagahora, K. Higashi, Mater. Sci. Eng. A **280**, 62 (2000)
9. R.M. Imayev, G.A. Salishchev, O.N. Senkov, V.M. Imayev, N.K. Gabdullin, M.R. Shagiev, A.V. Kuznetsov, F.H. Froes, Mater. Sci. Eng. A **300**, 263 (2001)
10. A. Belyakov, T. Sakai, H. Miura, K. Tsuzaki, Phios. Mag. A **81**, 2629 (2001)
11. Y.C. Chen, Y.Y. Huang, C.P. Chang, P.W. Kao, Acta Mater. **51**, 2005 (2003)
12. O. Sitdikov, T. Sakai, A. Goloborodko, H. Miura, Scr. Mater. **51**, 175 (2004)
13. P.J. Apps, M. Berta, P.B. Prangnell, Acta Mater. **53**, 499 (2005)
14. I. Mazurina, T. Sakai, H. Miura, O. Sitdikov, R. Kaibyshev, Mater. Trans. **50**, 101 (2009)
15. O. Sitdikov, T. Sakai, E. Avtokratova, R. Kaibyshev, Y. Kimura, K. Tsuzaki, Mater. Sci. Eng. A **444**, 18 (2007)
16. R.R. Mulyukov, R.M. Imayev, A.A. Nazarov, M.F. Imayev, V.M. Imayev, *Superplasticity of Ultrafine Grained Alloys: Experiment, Theory, Technologies* (Nauka, Moscow, 2014), p. 284 (in Russian)
17. O. Sitdikov, E. Avtokratova, T. Sakai, J. Alloys Compd. **648**, 195 (2015)
18. O. Sitdikov, R. Kaibyshev, Mater. Sci. Eng. A **328**, 147 (2002)
19. Y.A. Filatov, V.I. Yelagin, V.V. Zacharov, Mater. Sci. Eng. A **280**, 97 (2000)
20. Y. Zeng, Y. Chao, Z. Luo, Y. Cai, R. Song, High Temp. Mater. Process. **37**, 603 (2018)
21. Channel 5, User Manual, O. Instruments HKL (2007). http://web.archive.org/web/20200807101801/https://aarc.ua.edu/wp-content/uploads/docs/JEOL-7000FOxford_Channel_5_User_Manual.pdf
22. ISO Standard 13067, Microbeam Analysis—Electron Backscatter Diffraction—Measurement of Average Grain Size (2011)
23. P.B. Hirsch, A. Howie, R.B. Nicholson, D.W. Pashley, M.J. Whelan, *Electron Microscopy of Thin Crystals* (Butter Worths, London, 1965), p. 549
24. O.N. Senkov, M.R. Shagiev, S.V. Senkova, D.B. Miracle, Acta Mater. **56**, 3723 (2008)
25. E. Avtokratova, O. Sitdikov, M. Markushev, R. Mulyukov, Mater. Sci. Eng. A **538**, 386 (2012)
26. H.J. McQueen, S. Spigarelli, M.E. Kassner, E. Evangelista, *Hot Deformation and Processing of Aluminum Alloys* (CRC Press, Taylor & Francis Group, Boca Raton, 2011), p. 564
27. J.P. Poirier, *Creep of Crystals: High-Temperature Deformation Processes in Metals, Ceramics and Minerals* (Cambridge University Press, Cambridge, 1985), p. 260
28. M.E. McMahon, *The Variation of Subgrain Misorientation in Aluminum with Large Steady-State Creep Strain*. Thesis (M.S. in Mechanical Engineering), (Naval Postgraduate School, 1986), p. 72
29. P.J. Hurley, F.J. Humphreys, Acta Mater. **51**, 1087 (2003)
30. C. Kobayashi, T. Sakai, A. Belyakov, H. Miura, Phil. Mag. Lett. **87**, 751 (2007)
31. T. Sakai, A. Belyakov, H. Miura, Metal. Mat. Trans. A **39**, 2206 (2008)
32. O. Sitdikov, T. Sakai, H. Miura, C. Hama, Mater. Sci. Eng. A **516**, 180 (2009)
33. T. Takeshita, U.F. Kocks, H.-R. Wenk, Acta Metall. **37**, 2595 (1989)
34. S. Aris, R.V. Martins, V. Honkimaki, A. Pyzalla, Comput. Mater. Sci. **19**, 116 (2000)
35. M. Hatherly, A.S. Malin, Scr. Met. **18**, 449 (1984)
36. D.A. Hughes, N. Hansen, Metall. Trans. A **24**, 2021 (1993)
37. U. Chakkingal, P.F. Thomson, J. Mater. Process. Technol. **117**, 169 (2001)
38. I. Mazurina, T. Sakai, H. Miura, O. Sitdikov, R. Kaibyshev, Mater. Sci. Eng. A **486**, 662 (2008)
39. J. Čadek, *Creep in Metallic Materials* (Elsevier, New York, 1988), p. 372
40. E. Avtokratova, O. Sitdikov, O. Mukhametdinova, M. Markushev, S.V.S.N. Murty, M.J.N.V. Prasad, B.P. Kashyap, J. Alloys Compd. **673**, 182 (2016)
41. O. Sitdikov, E. Avtokratova, O. Mukhametdinova, R. Garipova, M. Markushev, Phys. Met. Metallogr. **118**, 1215 (2017)
42. H.J. McQueen, Metal Forum (Australia) **4**, 81 (1981)
43. O. Sitdikov, Inorg. Mater. Appl. Res. **7**, 149 (2016)
44. A. Russell, K.L. Lee, *Structure—Property Relations in Nonferrous Metals* (Wiley, New York, 2005), p. 440